12-1-2020

Structure Analysis of Natural Wangdaodeite—linbo3-Type fetio3

Oliver Tschauner
University of Nevada, Las Vegas, oliver.tschauner@unlv.edu

Chi Ma
Division of Geological and Planetary Sciences

Matthew G. Newville
The Advanced Photon Source

Antonio Lanzirotti
The Advanced Photon Source

minerals

MDPI

Article

Structure Analysis of Natural Wangdaodeite—$LiNbO_3$-Type $FeTiO_3$

Oliver Tschauner [1,*], Chi Ma [2], Matthew G. Newville [3] and Antonio Lanzirotti [3]

1 Department of Geoscience, University of Nevada Las Vegas, Las Vegas, NV 89154, USA
2 Division of Geology and Planetary Sciences, California Institute of Technology, Pasadena, CA 91125, USA; chima@caltech.edu
3 GeoSoilEnviroCARS, Argonne National Laboratory, University of Chicago at the Advanced Photon Source, Argonne, IL 60367, USA; newville@uchicago.edu (M.G.N.); lanzirotti@uchicago.edu (A.L.)
* Correspondence: oliver.tschauner@unlv.edu

Received: 29 October 2020; Accepted: 23 November 2020; Published: 30 November 2020

check for updates

Abstract: This paper reports the first structure refinement of natural wangdaodeite, $LiNbO_3$-type $FeTiO_3$ from the Ries impact structure. Wangdaodeite occurs together with recrystallized ilmenite clasts in shock melt veins which have experienced peak shock pressures of between 17 and 22 GPa. Comparison of natural and synthetic wangdaodeite points toward a correlation between the distortion of ferrate- and titanate-polyhedra and the c/a ratio of the unit cell. The Raman spectrum of wangdaodeite is calculated based on the refined structure. Comparison to the reported spectrum of the type-material shows that the Raman peak at 738–740 cm^{-1} is indicative for this phase, whereas other features in type-wangdaodeite are tentatively assigned to disordered ilmenite.

Keywords: high-pressure mineral; $LiNbO_3$; $FeTiO_3$; shock-compression

1. Introduction

$FeTiO_3$ is trimorph with ilmenite stable at ambient pressure; liuite [1], a $GdFeO_3$-type perovskite, stable above ~15–20 GPa [2–5]; and wangdaodeite, a $LiNbO_3$-type perovskite as intermediary phase [3,4,6,7]. The high-pressure phase transition of ilmenite to an intermediate structure prior to the formation of the $GdFeO_3$-type perovskite was first reported by Syono et al. [8] and Ito and Matsui [9]. These authors proposed this phase to assume the corundum-structure. Later, this phase was identified as $LiNbO_3$-type $FeTiO_3$ [3]. Assessment of phase boundaries through calorimetric data [10] and compression-decompression cycling [4,5] show that at least pure $LiNbO_3$-type $FeTiO_3$ has no stability field.

$LiNbO_3$-type $FeTiO_3$ can be conserved at ambient pressure and has found attention in solid state physics because of its multiferroic behavior [11].

$FeTiO_3$ in the $LiNbO_3$-structure has also been reported from nature. In 2009, the natural occurrence of this phase in shock-metamorphized gneiss from the Ries impact crater was announced in a conference abstract by Dubrovinsky et al. [12]. Xie et al. [6,7] reported the same phase from the Suizhou impact structure. Based on Xie et al.'s findings, $LiNbO_3$-type $FeTiO_3$ was approved as a mineral with the name "wangdaodeite" (IMA 2016-007 [6,7]).

Neither Dubrovinsky et al. [12] nor Xie et al. [6,7] presented structure analyses of natural $LiNbO_3$-type $FeTiO_3$. Xie et al. 2020 [7] showed by means of TEM–SAED (transmission electron microscopy–selected area electron diffraction) that the new mineral species is consistent with the $LiNbO_3$-structure. Here we present the first structure analysis of natural wangdaodeite based on synchrotron X-ray diffraction data and Rietveld refinement (Tables 1–3 and Supplementary Cif). Henceforth, $LiNbO_3$-type $FeTiO_3$ is called by its mineral name wangdaodeite in this paper.

2. Materials and Methods

2.1. Occurrence

The examined ilmenite and wangdaodeite occur as clasts in a shock melt vein in a xenolith of garnet-sillimanite-cordierite restite (thin section c of specimen ZLN114 [13]) that was found in suevite of Zipplingen, a locality in the Ries impact structure in S-Germany. The clasts were examined by field-emission scanning electron microscope (FE-SEM) with a ZEISS 1550VP field emission SEM at Caltech, synchrotron micro-X-ray diffraction (see below), and electron microprobe chemical analysis (see below) The petrography of ZLN114c was already discussed in Stähle et al. [13,14].

Figure 1a–c show the examined clasts and the surrounding host rock. The host rock consists of almandine-rich garnet, cordierite, and sillimanite, with ilmenite, rutile, "biotite" (annite-rich mica), fluorapatite, monazite-Ce, and zircon as accessory phases (Figure 1a). Baddeleyite was found in the shock melt vein and probably represents the decomposition of zircon or reidite. The shock melt vein is composed of a jadeite- and hedenbergite-like pyroxene. Clasts of trapped wall-rock minerals are partially or completely transformed or recrystallized. High-pressure minerals in trapped clasts are riesite (IMA 2015-110 [15]), akaogiite [15,16], reidite, and stishovite [13] pseudomorph after rutile, zircon, and quartz, respectively. Wangdaodeite and recrystallized ilmenite replace deformed ilmenite single-crystal clasts within or at the border of the shock melt vein. The crystallites of both phases of $FeTiO_3$ assume size mostly between 200 to 600 nm in diameter (Figure 1b,c), which is noticeably smaller than that reported for wangdaodeite type material (of 2–20 μm in diameter [7]). No indication of pressure-induced decomposition of $FeTiO_3$ into TiO_2 and $FeTi_2O_4$ post-rutile and post-spinel phases [17] was observed. This indicates that the peak shock pressure of ilmenite clasts in ZLN114c has been below 28 GPa. The clasts exhibit reaction halos which are composed of a sodic Ti-rich clinopyroxene, similar to those reported by Sirotkina et al. [18].

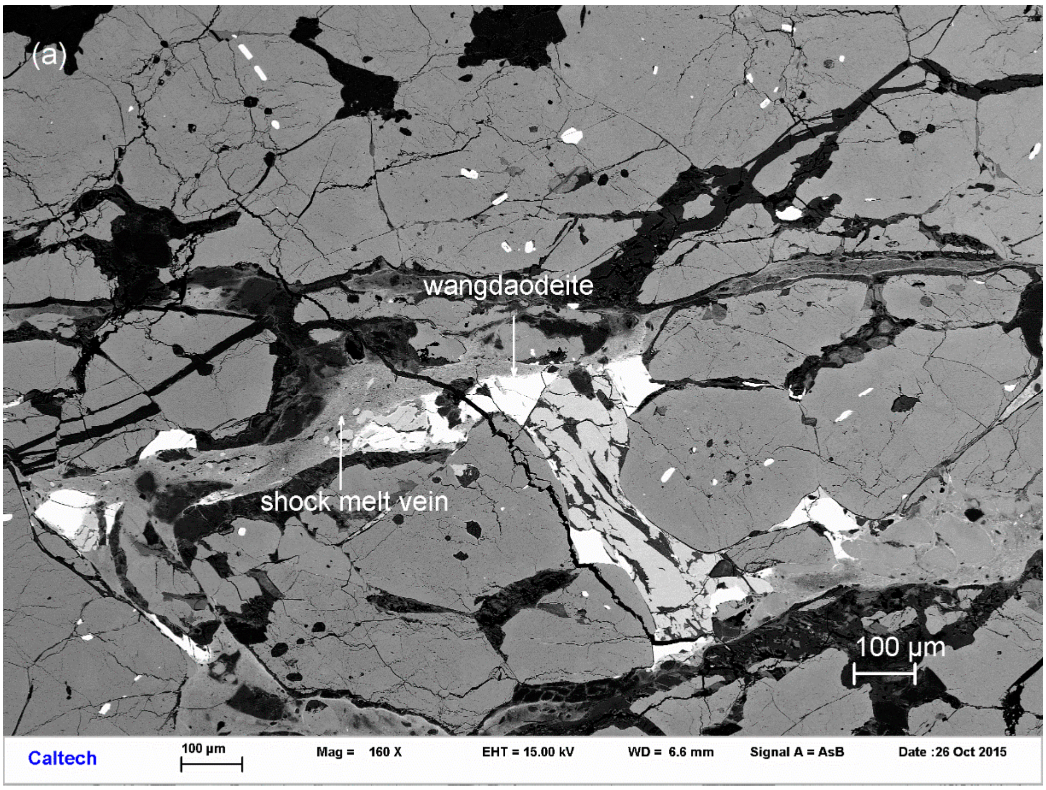

Figure 1. *Cont.*

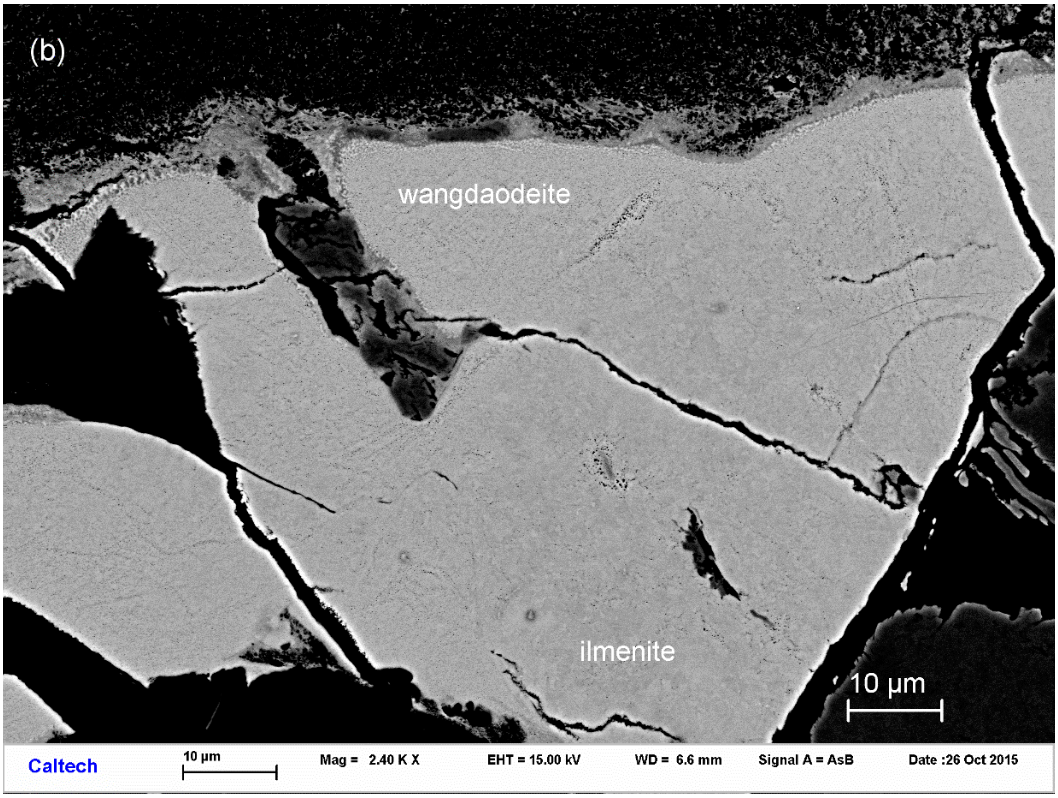

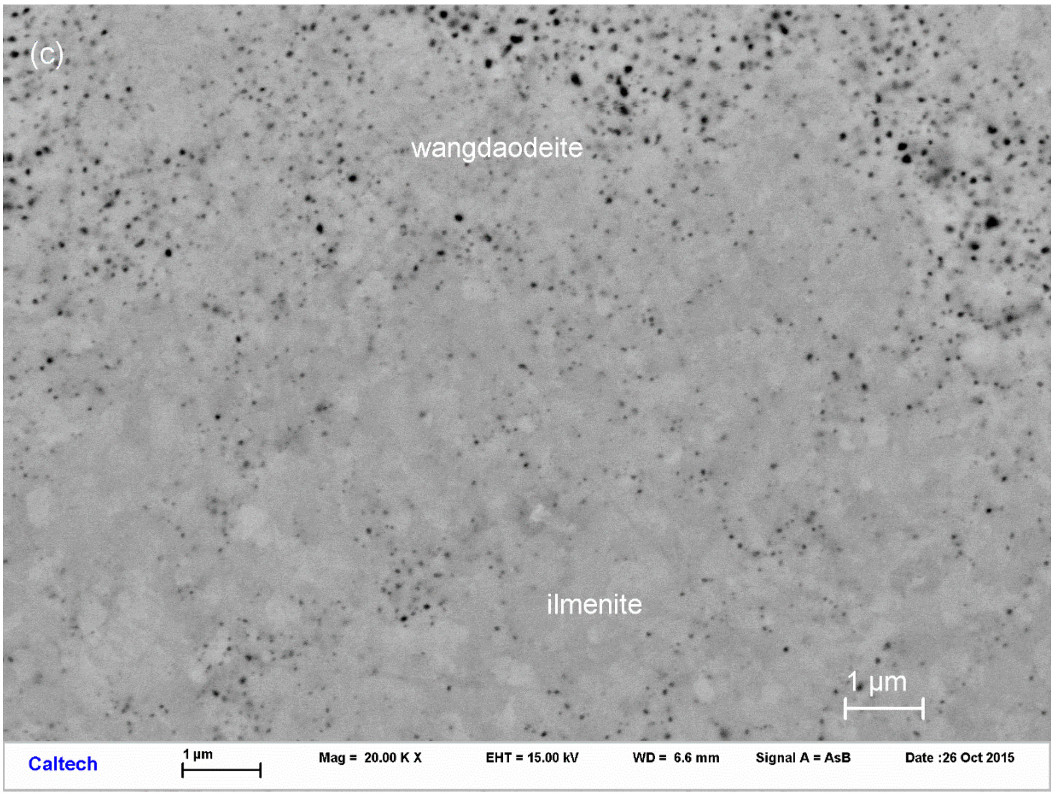

Figure 1. (**a**) SEM BSE image showing part of a wangdaodeite-bearing shock melt vein in Ries section ZLN114c; (**b**) enlarged BSE image of wangdaodeite and recrystallized ilmenite in contact with the shock melt vein; (**c**) a further enlarged BSE image showing individual crystallites of wangdaodeite and recrystallized ilmenite. The two minerals have the same composition within the resolution of the EPM analysis.

No spatial separation is noticeable between wangdaodeite and recrystallized ilmenite. The latter dominates by mass. Backscatter electron (BSE) contrast may reflect the density contrast between the two phases but could also reflect differences in electron density along different crystallite orientations of the same phase. It should be noted that not all ilmenite clasts have recrystallized completely. Some clasts exhibit recrystallization and the presence of wangdaodeite only at their rims where they contact shock melt. Only recrystallized areas contain wangdaodeite. No difference in the compositions of the two coexisting phases was observed. The average composition with an 8 mol% pyrophanite ($MnTiO_3$) component is very similar to that reported by Dubrovinsky et al. [12].

Ilmenite crystallites far from the shock melt vein are neither recrystallized nor show they any measurable diffraction signal of wangdaodeite. Instead, they exhibit strong deformation and twinning. Oscillation diffractograms show features equivalent to those of the precession diffractograms reported for experimentally shocked ilmenite [8]. Results were shown in Tables 1 and 2.

Table 1. Fractional atom coordinates, site fraction occupancies, and isotropic thermal displacement factors of wangdaodeite and recrystallized ilmenite from Ries xenolith ZLN114. The site fractional occupancies were fixed according to the chemical analysis. SFO = site fractional occupancy, Wyck. = Wyckoff site. Isotropic U in Å^2.

Wangdaodeite						
Atom	**Wyck.**	**SFO**	**x**	**y**	**z**	**U**
Fe1	6a	0.92	0	0	0.284(20)	0.015(1)
Mn1	6a	0.08	0	0	0.284(20)	0.015(1)
Ti1	6a	1	0	0	0.0012(15)	0.03(2)
O1	18b	1	0.3149(2)	0.025(20)	0.244(4)	0.003(1)
Ilmenite						
Atom	**Wyck.**	**SFO.**	**x**	**y**	**z**	**U**
Fe	6c	0.92	0	0	0.640(2)	0.0021(7)
Mn	6c	0.08	0	0	0.640(2)	0.0021(7)
Ti	6c	1	0	0	0.852(1)	0.0015(5)
O	18f	1	0.3149(2)	0.025(20)	0.244(4)	0.003(1)

Table 2. Unit cell dimensions and interatomic distances for wangdaodeite, synthetic $LiNbO_3$-type $FeTiO_3$, and for ilmenite.

Mineral	**V(Å^3)**	**a(Å)**	**c(Å)**	**c/a**	**Fe-O(Å)**	**Ti-O(Å)**
Wangdaodeite	313.3(5)	5.148(3)	13.649(2)	2.601(51)	2.215(24) 2.058(80)	2.111(31) 1.868(33)
Wangdaodeite [7]	314.1	5.13	13.78	2.69	-	-
Synthetic LN-type $FeTiO_3$ [19]	312.4(2)	5.127(1)	13.723(4)	2.627(1)	2.206(12) 2.063(32)	2.083(18) 1.888(13)
Synthetic LN-type $FeTiO_3$ [10]	311.3(3)	5.118(2)	13.723(4)	2.681(2)	-	-
Ilmenite [20]	314.6(2)	5.079(1)	14.082(5)	2.772(2)	2.2008(1) 2.0775(1)	2.0883(2) 1.8741(1)

2.2. *Analytical Methods*

Synchrotron X-ray diffraction, high-resolution SEM, electron back-scatter diffraction (EBSD), and electron microprobe analyses were used to characterize composition and structure. FE-SEM images are shown in Figure 1a–c. EBSD patterns of ilmenite and wangdaodeite are indiscriminable. Quantitative elemental microanalyses of the type material were carried out at Caltech using a JEOL 8200 electron microprobe operated at 15 kV and 20 nA in focused beam mode. Analyses were processed with the CITZAF correction on atomic number Z, absorption A, and fluorescence F. Analytical results are given in Table 3.

Table 3. Chemical analysis of wangdaodeite and ilmenite from Ries xenolith ZLN114c. The two minerals are not distinguishable by composition. The values are based on the average of the 12 point analyses.

Constituent	Wt.%	Range	SD	Probe Standard
TiO_2	52.48	52.11–52.71	0.17	TiO_2
FeO	43.09	42.71–43.63	0.25	fayalite
MnO	3.73	3.32–3.99	0.16	Mn_2SiO_4
MgO	0.04	0.02–0.07	0.01	forsterite
Total	99.34			

The empirical formula (based on 3 O atoms per formular unit) is $(Ti^{4+}{}_{1.00}Fe^{2+}{}_{0.91}Mn_{0.08})O_3$.

Diffraction data were collected at the undulator beamline 13-IDE (GSECARS, APS, Argonne National Laboratory) using a primary beam of wavelength at 0.61993 Å monochromatized by a four-crystal Si monochromator. The X-ray beam was focused on $2 \times 3\ \mu m^2$ by vertical and horizontal Kirkpatrick–Baesz mirrors of 200 mm focal length. The location of recrystallized ilmenite clasts in the shock –melt vein (Figure 1a–c) was determined by X-ray fluorescence mapping of the signal of the Kα lines of Fe, Ti, and Mn. A MAR 165 CCD area detector was used for collecting diffraction data. Diffraction data were collected in a forward scattering geometry. The patterns were recorded over a $20 \times 20\ \mu m^2$ map area with a grid size of 2 μm. The patterns were corrected for geometric distortion from detector tilt and integrated using Dioptas [21]. The diffraction patterns were smooth. Ilmenite exhibited minor texture (see Figure 2a) which we averaged by adding three patterns from different locations and which did not require fitting. Wangdaodeite did not exhibit any indications for preferred crystallite orientation.

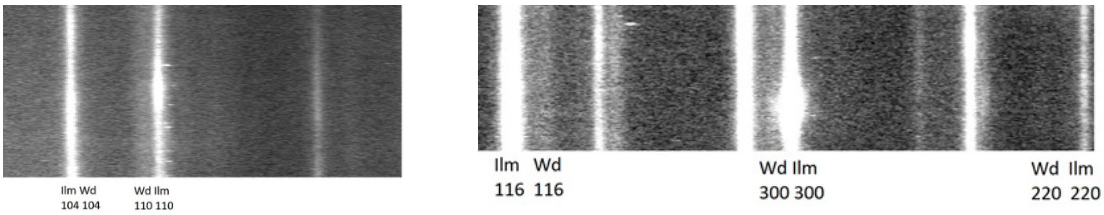

Figure 2. Diffractograms of ilmenite-wangdaodeite aggregates from Ries xenolith ZLN114c from the low angle and high angle range (left and right panel, respectively). Due to the noticeably different c/a ration, reflections of wangdaodeite occur at lower Bragg angles for the zone hk0 and at higher angles for hkl. Only fringes that are noticed as distinct already in the diffraction image are labeled. The entire set of observed Bragg reflections is shown in the integrated pattern in Figure 3 and given in Table 4. Interestingly, ilmenite exhibits some azimuthal intensity variations which indicate crystallite texture whereas diffraction of wangdaodeite does not exhibit deviations from random crystallite orientation. (**a**) Ilmenite; (**b**) Wangdaodeite.

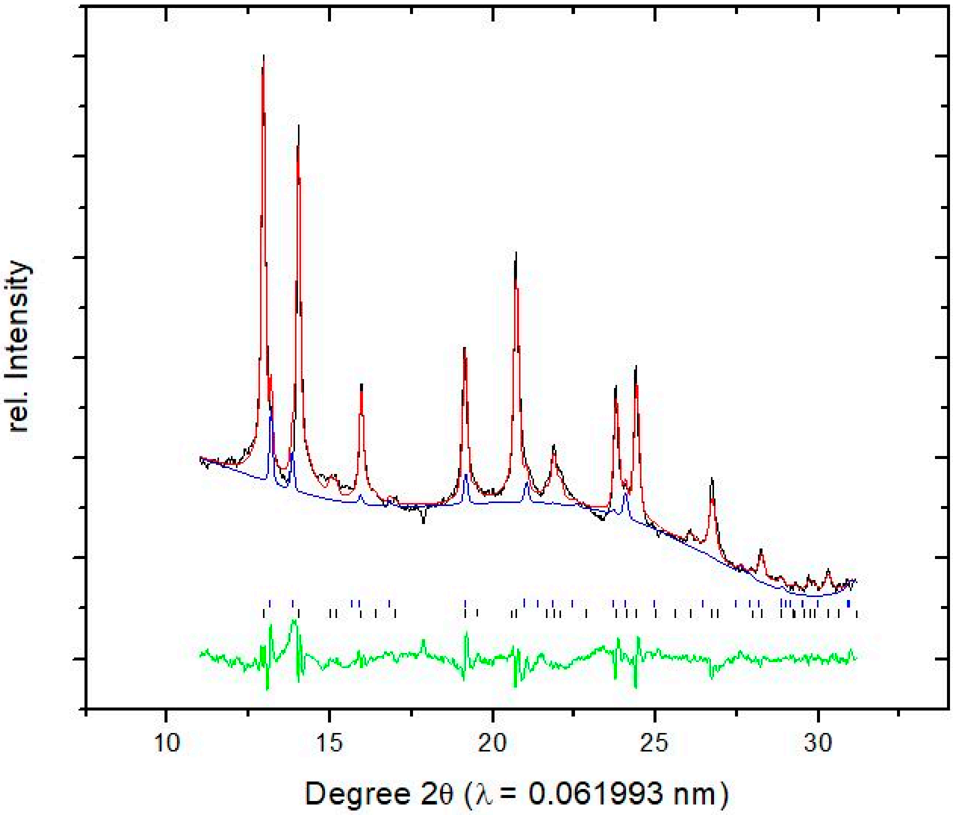

Figure 3. Integrated diffraction pattern of wangdaodeite and coexisting recrystallized ilmenite in a clast trapped in a shock-melt vein of Ries xenolith ZLN114. Black: Observed pattern. Red: Rietveld refined calculated pattern. Blue: Calculated refined pattern of wangdaodeite only. Green: Residual of fit. Blue and black tick marks indicate the Bragg angles of allowed reflections of wangdaodeite and ilmenite, respectively. Overlap of peaks of wangdaodeite with those of ilmenite and a structured background somewhat affect the quality of the refinement of wangdaodeite. However, the agreement of the R_{wP} of the Rietveld refinement with R_F indicates the absence of systematic errors in the structure refinement. The structured background is generated by the epoxy-resin that was used for impregnating the section.

Table 4. List of observed and calculated factor moduli of wangdaodeite. The R_F is 0.066.

h	k	l	mul	D	|Fcalc|	|Fexp|	D(|F|)
0	1	2	6	3.726	303.5	303.1	0.4
1	0	4	6	2.700	924.9	841.4	83.5
1	1	0	6	2.574	813.8	600.1	213.7
0	0	6	2	2.261	228.7	229.8	−1.1
1	1	3	12	2.237	355.4	362.3	−6.9
2	0	2	6	2.118	254.6	256.4	−1.8
0	2	4	6	1.863	885.7	861.0	24.7
1	1	6	12	1.699	630.7	677.9	−47.2
2	1	1	12	1.672	112.7	122.4	−9.7
1	2	2	12	1.635	174.5	185.6	−11.1
0	1	8	6	1.585	548.4	586.6	−38.2
2	1	4	12	1.509	683.2	702.0	−18.8
3	0	0	6	1.486	951.3	1000.0	−48.7
1	2	5	12	1.431	92.1	89.8	2.3
2	0	8	6	1.350	415.9	431.5	−15.6
1	1	9	12	1.301	188.2	185.1	3.1
1	0	10	6	1.298	574.8	575.0	−0.2

Table 4. *Cont.*

h	k	l	mul	D	|Fcalc|	|Fexp|	D(|F|)
2	2	0	6	1.287	547.3	582.0	−34.7
2	1	7	12	1.272	77.3	85.3	−8.0
3	0	6	6	1.242	200.6	218.8	−18.2
0	3	6	6	1.242	205.1	223.3	−18.2
2	2	3	12	1.238	142.8	149.5	−6.7
1	3	1	12	1.231	100.2	103.9	−3.7
3	1	2	12	1.217	162.5	171.1	−8.6
1	2	8	12	1.195	381.7	411.9	−30.2

3. Results

Debye fringes of wangdaodeite reflections are clearly observable as shoulders on the fringes of ilmenite and in between ilmenite fringes (Figure 2).

We used the structure of synthetic $LiNbO_3$-type $FeTiO_3$ as the starting model [19]. Ilmenite and wangdaodeite were refined simultaneously with the Rietveld method. After final convergence to R_{wp} = 0.065, χ^2 = 27.9 for 1440 observations, 9–10 vol% of the examined area were wangdaodeite, 90–91 vol% ilmenite.

Initial refinement was hampered by a structured background caused by the epoxy-resin impregnation of the thin section. Therefore, we repeated the Rietveld refinement [22] by reducing the 2ϑ range from between 5° and 32° to between 10° and 32°, thereby obtaining a smoother background along with a smaller number of fitting parameters. This second refinement was for 1151 observations and gave a final R_{wp} = 0.063, χ^2 = 26.3. The measures of goodness of fit are not much different from those above because of the overall large background signal which dominates the weighted whole pattern refinement parameter (Figure 3). However, the R_F for the extracted |F(hkl)| improved from 0.11 to 0.066 and this shows that the better background fit improved the assessment of |F(hkl)| significantly (see below).

Peak profiles of ilmenite show symmetric, broad, weak contributions which cannot be fitted with a single profile. Instead, we fitted these weak features as a separate fine-grained fraction of ilmenite. This approach improved refinement significantly and, thus, appears to represent a real bimodal distribution with grain size maxima around 60–90 and 5–10 nm, based on the Scherrer equation.

The final converged modeled pattern and the integrated diffraction pattern is shown in Figure 3. Overlap of ilmenite peaks with wangdaodeite reflections 114, 110, and 116 are marked. Therefore, we conducted a LeBail extraction [22] which converged to R_p = 0.038. The extracted |F(hkl)| were used for reversed Monte Carlo modeling of the structure of wangdaodeite in local optimization [23]. The optimization converged to R_F = 0.066. Observed and calculated |F(hkl)| are given in Table 4. We note that the deviations between observed and calculated |F(hkl)| are on the level of the residual of the Rietveld fit (Figure 3). Thus, there are no significant systematic errors in the structure model (which would be indicated if ΔF(hkl) would be generally smaller than the residual of peak fitting).

The refined crystallographic parameters are given in Table 1 and as Supplementary Cif Files. Bond distances and unit cell dimensions are given in Table 2.

4. Discussion

The structures of ilmenite and wangdaodeite are based on the corundum structure where edge-sharing octahedra form sheets with every third octahedral site left empty such that the occupied octahedra establish six-membered rings. The sheets are normal to 001. In wangdaodeite, each sheet is composed of ferrate- and titanate-octahedra, instead of alternating ferrate- and titanate-sheets as in ilmenite. Hence, the transition between ilmenite and wangdaodeite itself appears as a result of a sublattice shift of half of the face-sharing octahedral dimers which are perpendicular to 001. It should be noted that the two shortest group-subgroup chains are from R-3 → R3 → R3c and from R-3 → R-3c (corundum) → R3c and both involve the rearrangement of the O-sublattice. This suggests that the transition is achieved not through brute bond breaking by relative translation of the dimer chains but mediated by O-sublattice rearrangement between shallow potential wells where the displacement of cations is correlated with oxygen.

In a rigid sphere model and with equal ionic radii of Fe and Ti, there would be no difference in volume between the two arrangements. Instead, the bond distances of the ferrate-octahedra are larger than those in the higher charged titanate-octahedra and in consequence the arrangement of mixed titanate-ferrate layers reduces the volume over an arrangement of alternating pure titanate- and ferrate-layers where the total volume is controlled by the volume of the ferrate-sheets. An important parameter in this volume reduction is the anisotropic contraction of the ferrate octahedra (recte: trigonal scalenoeder combined with trigonal base planes). The distortion of the octahedra is anisotropic and consequently, the c/a ratio of wangdaodeite is smaller than that of ilmenite [10,19]. The volume effect is not large: it is 1.3% (Table 2, synthetic pure material: 1.5% [19] to 2% [10]). For comparison, the difference in the molar volume of ilmenite and liuite ($FeTiO_3$-perovskite) is 11% at standard conditions [5]. The average reduction of volume of pressure-driven phase transitions between 0.1 and 200 GPa is 11% at standard conditions [24].

In wangdaodeite from the Ries, the Ti-O distances of 2.111(31) and 1.868(33) (ratio = 1.13(3)) are slightly larger than in ilmenite (2.0883(2) and 1.8741(1), ratio = 1.114 [20], see Table 2) and the largest dilatation is along the longer apex with +0.042(10) Å. The change in bond distances of the titanate units between ilmenite and wangdaodeite is Δ(Ti-O) = +0.022(23) and −0.006(16) at standard conditions. Thus, within uncertainties bond distances overlap but tentatively, the titanate polyhedra approach the ferrate polyhedra in shape and anisotropy. This is plausible, considering that wangdaodeite contains both polyhedra in each sheet.

Fe-O bond distances in wangdaodeite are tentatively also more anisotropic than in ilmenite with 2.215(20) and 2.058(80) Å (ratio = 1.076(50), ilmenite: 2.2008(1) and 2.0775(1) Å, ratio = 1.059 [20], Table 2) but overlap within uncertainties. The long Fe-O distance is larger than in ilmenite. In sum, in wangdaodeite, the interatomic distances are at least partially longer than in ilmenite and this effect is compensated by a more pronounced distortion. Unfortunately, the uncertainties of the bond distances in wangdaodeite do not allow for a more quantitative assessment. Interestingly in synthetic, pure wangdaodeite [19] the Fe- and Ti-O bond distances are nearly indiscriminable from those of ilmenite (Table 2). This discrepancy is plausibly reflecting a real difference rather than a systematic error: The structure imposes strong constraints on bond distances through corner-sharing of face-sharing ferrate- and titanate units. Consequently, a relative change in the long and short apical distances within these units should express itself directly in a change of the c/a ratio. This is actually the case (Table 2): the synthetic wangdaodeite of Wu et al. [19] exhibits c/a = 2.676(1) whereas the present natural wangdaodeite from the Ries has c/a = 2.601(51). The volume is almost the same. This suggests that increasing distortion of the polyhedral units does not provide a significant gain in volume, although the c/a ratio of wangdaodeite does decrease with pressure with a weaker slope than that of ilmenite [19].

In sum, wangdaodeite falls well into the category of intermediate-pressure minerals which are distinguished from genuine high-pressure minerals through the absence of major bond rearrangements and changes in bond character [25]. Intermediate-pressure minerals gain volume through sterical rearrangements of polyhedral units. In wangdaodeite, the net volume gain is the result of a correlated distortion of polyhedral units along with a rearrangement of these units from alternating to mixed TiO_6- and FeO_6-polyhedra through sublattice translation. Since the arrangement of the face- and corner-sharing XO_6-units is already quite compact, equivalent to a two-third filling of an hcp-type lattice, the volume reduction is small.

Ilmenite has 12 optical modes which are equally Raman- and infrared-active because of the absence of inversion symmetry in the crystal lattice: $\Gamma = 4A_{g,u} + 8E_{g,u}$ (using the algorithm described in [26]). We use an observed Raman spectrum of ilmenite (Rruff #06149) to adjust force-constants for the Fe-O and Ti-O bonds. It is understood that the intensity of the Raman peaks cannot be predicted with a force-constant model [27]. Wangdaodeite has 12 Raman- and IR-active modes $\Gamma = 4A_1 + 8E$ [26]. Using the same set of force constants, we predict the energy of the Ti-O stretching vibration shifted from 720–730 to ~790 cm^{-1} (Table 5). Thus, wangdaodeite should be observable and discriminable from ilmenite in the Raman spectrum by peaks at these two energies, given their intensity is measurable. It should be noted that the equal energies of different modes of the same symmetry in wangdaodeite are a consequence of the simplicity of the model which does not take into account the distortions of bond angles. Similarly, the low-energy modes which have were observed in ilmenite are not quantitatively assessed here because these modes involve bond angle distortion. Therefore, no modes below 270 cm^{-1} are listed in Table 5.

Table 5. Raman and IR-active bands of ilmenite, defective ilmenite, and wangdaodeite above 270 cm^{-1}. Energies are given in cm^{-1}. The * marks silent modes. In brackets: ilmenite observed, Rruff #06149. Data for type wangdaodeite and coexisting shocked ilmenite are taken from Xie et al. [7].

Mode Symmetry	Ilmenite	Ilmenite (Defective)	Type-Wangdaodeite + Ilmenite	Mode Symmetry	Wangdaodeite
A_g (A_u)	722 (727)	763	**738–740**	A_1	**736 ± 10**
-	-	-	-	A_1	**736 ± 10**
A_g (A_u)	**371 (369)**	**371**	**372**	-	-
A_g (A_u)	-	**281 ***	**273–276**	-	-
A_u	-	**695 ***	**686–690**	-	-
A_u	-	959 *	-	-	-
-	- (598)	-	560–563	-	-
E_g (E_u)	**679 (680)**	689	**681**	E	788 ± 10
E_g (E_u)	340 (350)	340	332	E	788 ± 10

Bold: Matched observed and calculated mode energies.

The reported Raman spectra of type wangdaodeite and ilmenite [7] show, indeed, a pronounced peak at 738–740 cm^{-1} which matches the calculated A_1-mode of wangdaodeite (736 cm^{-1} ± 10 cm^{-1}). Other modes in the observed spectra belong to ilmenite (Table 5). However, the observed peaks at 273–276 cm^{-1} and 686–690 cm^{-1} are clearly not from ilmenite nor do they match the calculated spectrum of wangdaodeite. The latter has several shortcomings, and it cannot be excluded that the second A_1 mode is as low as 686–690 cm^{-1}. While this cannot be tested with the given limited model, we introduced a structural defect in ilmenite by placing some O on site 3a and reducing the occupancy of site 18f accordingly. In terms of difference from other structural modifications of ilmenite, this change does not cause additional peaks in the powder diffraction pattern and only modestly changes intensities of the observed peaks: an additional Rietveld refinement that includes this defective ilmenite is almost insignificantly different from that of regular ilmenite (R_{wP} = 0.065). The additional O minority site establishes a Ti-O bond of about 2.0 Å length, which is compensated by an O-deficit in the regular TiO_6-polyhedron. This change, minor in the diffraction pattern, generated additional Raman shifts which are close to the observed ones (Table 5). The Raman peaks at 273–276 cm^{-1} and 686–690 cm^{-1} correspond to silent modes in the extended phonon spectrum of ilmenite but because these modes are correlated with partially occupied sites, they exhibit Raman- and IR-activity through local symmetry breaking. We suggest structural defects in ilmenite as an alternative model that explains these two Raman peaks in the spectrum of type-wangdaodeite.

It is an interesting and, in several aspects, useful side-effect in shock-generated transformations that they occasionally arrest intermediate states of major transitions which under static conditions are only seen in their final states [24,25,28–30]. Ilmenite in xenolith ZLN114 of impacted bedrock from the Ries has experienced a peak shock pressure in the range of 19 ± 3 GPa [14,15]. Along the principal Hugoniot of ilmenite, the temperature is insufficient to induce the transformation of ilmenite into its stable high-pressure polymorph liuite [8]. On a laboratory time scale, this transition appears to occur around 50 GPa [31]. However, ilmenite clasts bordering at or trapped within shock melt veins likely underwent this transformation which occurs at 15–20 GPa static pressure [4,5]. The effect of temperature is evident from the thorough recrystallization of the heated clasts (Figure 1c) whereas ilmenite afar from the melt veins is highly deformed but has overall retained its original crystal orientation. Wangdaodeite is plausibly the product of incomplete back-transformation of liuite into ilmenite upon release from dynamic compression. At least its formation upon release of static pressure and temperature of liuite was experimentally observed [4,5]. Nanocrystalline ilmenite that occurs within the ilmenite-wangdaodeite aggregates is plausibly the product of continuing back-transformation of wangdaodeite into ilmenite at low to ambient temperature and over geologic time. The Ries impact occurred 14.8(2) Ma ago [32].

5. Conclusions

We present the first structure analysis of wangdaodeite, natural $FeTiO_3$ in the $LiNbO_3$-type structure. Wangdaodeite from a xenolith in suevite of the Ries impact structure was used for this analysis. In wangdaodeite, each octahedral sheet contains titanate- and ferrate-units and, in consequence, these units are more distorted than in ilmenite. In synthetic wangdaodeite, the Fe-O and Ti-O interatomic distances are within uncertainties, nearly indiscriminable from those in ilmenite whereas in natural wangdaodeite they are slightly but systematically larger and the small volume contraction during the phase transition is the result of the distortion of the polyhedra. The difference between synthetic and natural wangdaodeite appears to be systematic and is reflected in the change of the c/a ratio, which is strongly constrained by the polyhedral distortion.

Based on the structure, we calculate Raman- and IR-active modes for wangdaodeite and compare them with the reported spectrum of the type-material. We find that the Raman peak at 738–740 cm^{-1} in the spectrum of type-wangdaodeite is clearly from this phase and can serve as an indicator in Raman studies. Other features in the Raman spectrum of type-wangdaodeite are potentially from ilmenite with a partial structural disorder.

It is noteworthy that wangdaodeite, the metastable $LiNbO_3$-type polymorph of $FeTiO_3$, was conserved over 14.8 Ma at ambient temperature. We suggest that doping of $FeTiO_3$ with a few mol% of $MnTiO_3$ increases the kinetic barrier for back-transformation into ilmenite and opens a pathway of synthesis of this interesting multiferroic material [11].

Supplementary Materials: The following are available online at http://www.mdpi.com/2075-163X/10/12/1072/s1, wangdaodeite.cif document.

Author Contributions: Conceptualization, O.T. and C.M.; methodology, O.T., C.M., A.L. and M.G.N.; software, M.G.N.; validation, O.T. and C.M.; formal analysis, O.T. and C.M.; investigation, O.T., C.M. and A.L.; resources, C.M., A.L. and M.G.N.; data curation, O.T. and C.M.; writing—original draft preparation, O.T.; writing—review and editing, O.T. and C.M.; funding acquisition, O.T., A.L. and M.G.N. All authors have read and agreed to the published version of the manuscript.

Funding: Part of this work was supported by DOE Cooperative Agreement #DE-NA0001982, DOE-contract.DE-FG02-94ER14466, and NSF Grants EAR-1634415, -1128799, -1322082, and DMR-0080065.

Acknowledgments: The Advanced Photon Source, a DOE Office of Science User Facility is operated by Argonne National Laboratory under Contract No. DE-AC02-06CH11357. SEM and EPMA measurements were carried out at the Geological and Planetary Science Division Analytical Facility at Caltech, supported in part by NSF grants EAR-0318518, EAR-1322082, and DMR-0080065. O.T. acknowledges the support from DOE Cooperative Agreement #DE-NA0001982We also thank V. Stähle and D. Stöffler for providing the thin-section ZLN114c which contains type riesite and we thank the Institut für Geowissenschaften, University of Heidelberg, and in particular M. Trieloff for permitting us to examine this section, which is part of their collection.

Conflicts of Interest: The authors declare no conflict of interest.

References

1. Ma, C.; Tschauner, O. Liuite, IMA 2017-042a. *CNMNC Newsl.* **2018**, *46*, 1189, reprinted in *Eur. J. Mineral.* **2018**, *30*, 1181–1189.
2. Liu, L. High-pressure phase transformations and compression of ilmenite and rutile, I. Experimental results. *Phys. Earth Planet. Inter.* **1975**, *10*, 167–176. [CrossRef]

3. Leinenweber, K.; Utsumi, W.; Tsuchida, Y.; Yagi, T.; Kurita, K. Unquenchable high-pressure perovskite polymorphs of $MnSnO_3$ and $FeTiO_3$. *Phys. Chem. Miner.* **1991**, *18*, 244–250. [CrossRef]
4. Ming, L.C.; Kim, Y.-H.; Uchida, T.; Wang, Y.; Rivers, M. In situ X-ray diffraction study of phase transitions of $FeTiO_3$ at high pressures and temperatures using a large-volume press and synchrotron radiation. *Am. Miner.* **2006**, *91*, 120–126. [CrossRef]
5. Nishio-Hamane, D.; Zhang, M.; Yagi, T.; Ma, Y. High-pressure and high-temperature phase transitions in $FeTiO_3$ and a new dense $FeTi_3O_7$ structure. *Am. Miner.* **2012**, *97*, 568–572. [CrossRef]
6. Xie, X.; Gu, X.; Yang, H.; Chen, M.; Li, K. Wangdaodeite, IMA 2016-007. *CNMNC Newsl.* **2016**, *31*, 695, reprinted in *Mineral. Mag.* **2016**, *80*, 691–697.
7. Xie, X.; Gu, X.; Yang, H.; Chen, M.; Li, K. Wangdaodeite, the $LiNbO_3$-structured high-pressure polymorph of ilmenite, a new mineral from the Suizhou L6 chondrite. *Meteorit. Planet. Sci.* **2020**. [CrossRef]
8. Syono, Y.; Yamauchi, H.; Ito, A.; Someya, Y.; Ito, E.; Matsui, Y.; Akaogi, M.; Akimoto, S.-I. Magnetic properties of the disordered ilmenite $FeTiO_3$ II synthesized at very high pressure. In Proceedings of the Ferrites: Proceedings of the International Conference, Kyoto, Japan, 29 September–2 October 1980; pp. 192–195.
9. Ito, E.; Matsui, Y. High-pressure transformations in silicates, germanates, and titanates with ABO_3 stoichiometry. *Phys. Chem. Miner.* **1979**, *4*, 265–274. [CrossRef]
10. Mehta, A.; Leinenweber, K.; Navrotsky, A.; Akaogi, M. Calorimetric study of high-pressure polymorphism in $FeTiO_3$—stability of the perovskite phase. *Phys. Chem. Miner.* **1994**, *21*, 207–212. [CrossRef]
11. Varga, T.; Kumar, A.; Vlahos, E.; Denev, S.; Park, M.; Hong, S.; Sanehira, T.; Wang, Y.; Fennie, C.J.; Streffer, S.K.; et al. Coexistence of Weak Ferromagnetism and Ferroelectricity in the High Pressure $LiNbO_3$-Type Phase of $FeTiO_3$. *Phys. Rev. Lett.* **2009**, *103*, 047601. [CrossRef]
12. Dubrovinsky, L.S.; El Goresy, A.; Gillet, P.; Wu, X.; Simionivici, A. A novel natural shock-induced high-pressure polymorph of $FeTiO_3$ with the Li-niobate structure from the Ries Crater, Germany. *Met. Planet. Sci.* **2009**, *44*, A64.
13. Stähle, V.; Altherr, R.; Nasdala, L.; Ludwig, T. Ca-rich majorite derived from high-temperature melt and thermally stressed hornblende in shock veins of crustal rocks from the Ries impact crater (Germany). *Contrib. Miner. Pet.* **2011**, *161*, 275–291. [CrossRef]
14. Stähle, V.; Altherr, R.; Nasdala, L.; Trieloff, M.; Varychev, A. Majoritic garnet grains within shock-induced melt veins in amphibolites from the Ries impact crater suggest ultrahigh crystallization pressures between 18 and 9 GPa. *Contrib. Miner. Pet.* **2017**, *172*, 86. [CrossRef]
15. Tschauner, O.; Ma, C.; Lanzirotti, A.; Newville, M.G. Riesite, A new high pressure polymorph of TiO_2 from the Ries impact structure. *Minerals* **2020**, *10*, 78. [CrossRef]
16. El Goresy, A.; Dubrovinsky, L.; Gillet, P.; Graup, G.; Chen, M. Akaogiite: An ultra-dense polymorph of TiO_2 with the baddeleyite-type structure, in shocked garnet gneiss from the Ries Crater, Germany. *Am. Miner.* **2010**, *95*, 892–895. [CrossRef]
17. Akaogi, M.; Abe, K.; Yusa, H.; Ishii, T.; Tajima, T.; Kojitani, H.; Mori, D.; Inaguma, Y. High-pressure high-temperature phase relations in $FeTiO_3$ up to 35 GPa and 1600 A degrees C. *Phys. Chem. Miner.* **2017**, *44*, 63–73. [CrossRef]
18. Sirotkina, E.A.; Bobrov, A.V.; Spivak, A.V.; Bindi, L.; Pushcharovsky, D.Y. X-ray single-crystal and Raman study of $(Na_{0.86}Mg_{0.14})(Mg_{0.57}Ti_{0.43})Si_2O_6$, a new pyroxene synthesized at 7 GPa and 1700 degrees C. *Phys. Chem. Miner.* **2016**, *43*, 731–738. [CrossRef]
19. Wu, X.; Steinle-Neumann, G.; Narygina, O.; McCammon, C.; Dubrovinsky, L. In situ high-pressure study of $LiNbO_3$-type $FeTiO_3$: X-ray diffraction and Mössbauer spectroscopy. *High Press. Res.* **2010**, *30*, 395–405. [CrossRef]
20. Wechsler, B.A.; Prewitt, C.T. Crystal structure of ilmenite ($FeTiO_3$) at high temperature and at high pressure. *Am. Miner.* **1984**, *69*, 176–185.
21. Prescher, C.; Prakapenka, V.B. DIOPTAS: A program for reduction of two-dimensional X-ray diffraction data and data exploration. *High Press. Res.* **2015**, *35*, 223–230. [CrossRef]
22. Kraus, W.; Nolze, G. PowderCell—A program for the representation and manipulation of crystal structures and calculation of the resulting X-ray powder patterns. *J. Appl. Cryst.* **1996**, *29*, 301–303. [CrossRef]
23. Putz, H.; Schon, J.C.; Jansen, M. Combined method for ab initio structure solution from powder diffraction data. *J. Appl. Cryst.* **1999**, *32*, 864–870. [CrossRef]

24. Tschauner, O. Empirical constrains on volume changes in pressure-induced solid state transformations. *High Press. Res.* **2020**, *40*, 511–524.
25. Tschauner, O. High-pressure minerals. *Am. Miner.* **2019**, *104*, 1701–1731. [CrossRef]
26. Kroumova, E.; Aroyo, M.I.; Perez-Mato, J.M.; Kirov, A.; Capillas, C.; Ivantchev, S.; Wondratschek, H. Bilbao Crystallographic Server : Useful Databases and Tools for Phase-Transition Studies. *Phase Transit.* **2003**, *76*, 155–170. [CrossRef]
27. Dowty, E. Fully automated microcomputer calculation of vibrational spectra. *Phys. Chem. Miner.* **1987**, *14*, 67–79. [CrossRef]
28. Luo, S.-N.; Tschauner, O.; Asimow, P.D.; Ahrens, T.J. A new dense silica polymorph: A possible link between tetrahedrally and octahedrally coordinated silica. *Am. Miner.* **2004**, *89*, 455–461. [CrossRef]
29. Xie, X.; Sharp, T.J. A new mineral with an olivine structure and pyroxene composition in the shock-induced melt veins of Tenham L6 chondrite. *Am. Miner.* **2011**, *96*, 430–436. [CrossRef]
30. Tschauner, O.; Ma, C.; Spray, J.G.; Greenberg, E.; Prakapenka, V.B. Stöfflerite, $(Ca,Na)(Si,Al)_4O_8$ in the hollandite structure: A new high-pressure polymorph of anorthite from martian meteorite NWA 856. *Am. Miner.* **2020**, in print. [CrossRef]
31. King, D.A.; Ahrens, T.J. Shock compression of ilmenite. *J. Geophys. Res.* **1976**, *81*, 931–935. [CrossRef]
32. Schmieder, M.; Kennedy, T.; Jourdan, F.; Buchner, E.; Reimold, W.U. A high-precision ^{40}Ar-^{39}Ar age for the Nördlinger Ries impact crater, Germany, and implications for the accurate dating of terrestrial impact events. *Geochim. Cosmochim. Acta* **2018**, *220*, 146–157. [CrossRef]

Publisher's Note: MDPI stays neutral with regard to jurisdictional claims in published maps and institutional affiliations.